Article

Monodisperse PdBi Nanoparticles with a Face-Centered Cubic Structure for Highly Efficient Ethanol Oxidation

Xianzhuo Lao,[||] Min Yang,[||] Xiaoli Sheng, Jing Sun, Yiqian Wang,* Derui Zheng, Mingyuan Pang, Aiping Fu,* Hongliang Li, and Peizhi Guo*

Cite This: *ACS Appl. Energy Mater.* 2022, 5, 1282−1290

Read Online

ACCESS | Metrics & More | Article Recommendations | Supporting Information

ABSTRACT: Alloyed Pd-based nanocatalysts are considered as highly active fuel cell anodes toward the ethanol oxidation reaction (EOR). However, challenges remain in synthesizing free-standing monodisperse nanoparticles (NPs) with outstanding mass activity and long-term stability. In this work, PdBi NPs are synthesized by a one-step oil bath method with controllable sizes and compositions. The doping of Bi displays a positive effect on the oxidation of ethanol. The Pd_8Bi NPs with an average size of 9.0 nm are found to possess an exceptional electrocatalytic mass activity with superior antitoxic ability and outstanding long-term stability toward EOR. These are mainly attributed to the change in the electronic structure and the *d*-band center of Pd, increase of the interatomic distance within a unit cell, and large electrochemically active surface area values, with lots of reaction sites provided by the morphology-optimized NPs. Higher electrocatalytic temperatures, higher pH values, and higher concentrations of C_2H_5OH accelerate each step of electro-oxidation on EOR. The density functional theory calculations demonstrate that the energy barrier of PdBi NPs can be reduced by adjusting the Bi content, resulting in excellent electrocatalytic activity toward EOR. This work provides a promising strategy to prepare monodisperse PdM alloys as efficient catalysts for fuel electro-oxidation.

KEYWORDS: palladium-bismuth, nanoparticles, ethanol oxidation, electrocatalysis, DFT
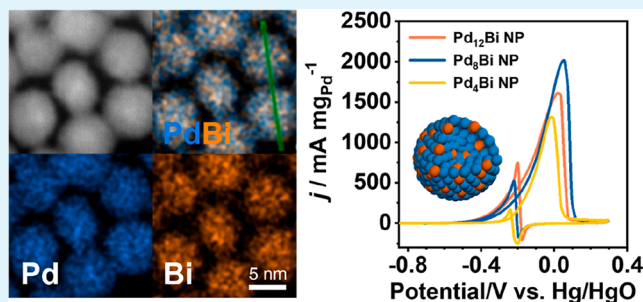
1. INTRODUCTION

In comparison with fossil fuels that convert thermal energy to mechanical energy, the efficiency of which is limited by the Carnot cycle, direct ethanol fuel cells (DEFCs) display excellent electrocatalytic performance by directly converting the ethanol fuel into electricity.[1−4] In addition, DEFCs with features of low toxicity and low cost are regarded as green power sources with high theoretical mass energy density (8 kW h kg^{-1}), low carbon emission, as well as stable conversion efficiency.[5−8]

To further improve the efficiency of DEFCs, designing highly efficient and stable catalysts becomes more urgent. Compared with gold and platinum, palladium (Pd) is considered a better candidate for the ethanol oxidation reaction (EOR) because Pd has the advantages of CO poisoning tolerance and low cost.[9−11] Instead of pure metals, alloying Pd with other metals can not only decrease the amount of Pd but also increase the performance. Lots of studies have been conducted to establish nanostructures for alloyed PdM (M = Ag, Cu, Pb, Co, Sn, Bi, etc.) as high-efficient catalysts toward the oxidation of ethanol, ascribed to the ensemble effects, geometric effects, and electronic effects.[12−17] Such effects allow the binding strengths of the reactants, intermediates, and products to optimal values, thus boosting the intrinsic activity of Pd.[10,18−21]

Alloys like PdBi NPs have emerged as excellent electrocatalysts, especially with unique antitoxic features and good durability, demonstrating the positive effects of Bi. Hall et al. reported the room-temperature synthesis of $Pd_{31}Bi_{12}$ nanostructures with porous morphology by the electrodeposition method for the oxygen reduction reaction.[17] Atanassov et al. synthesized bimetallic Pd_xBi materials with a sponge-like structure by the sacrificial support method for the glycerol oxidation reaction.[22] However, the synthesis of monodisperse alloys in a simple way remains a great challenge as the bismuth precursor is easily hydrolyzed to form bismuth oxides and bismuth hydroxides.[23,24] The good electron interactions between palladium and bismuth, and monodisperse alloyed PdBi NPs, can expose abundant electrochemically active sites for the electrocatalytic oxidation of ethanol.[25] These greatly
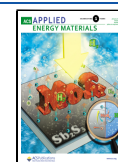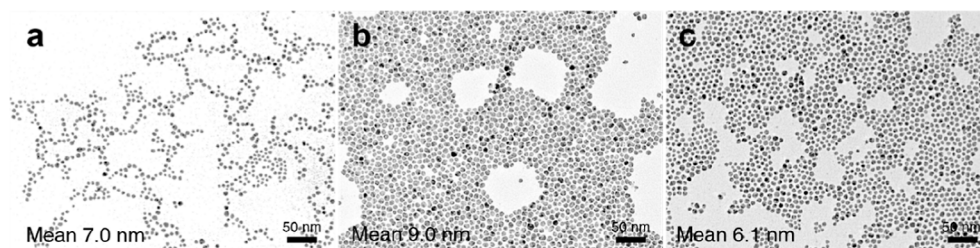
Figure 1. TEM images of $Pd_{12}Bi$ NPs (a), Pd_8Bi NPs (b), and Pd_4Bi NPs (c).
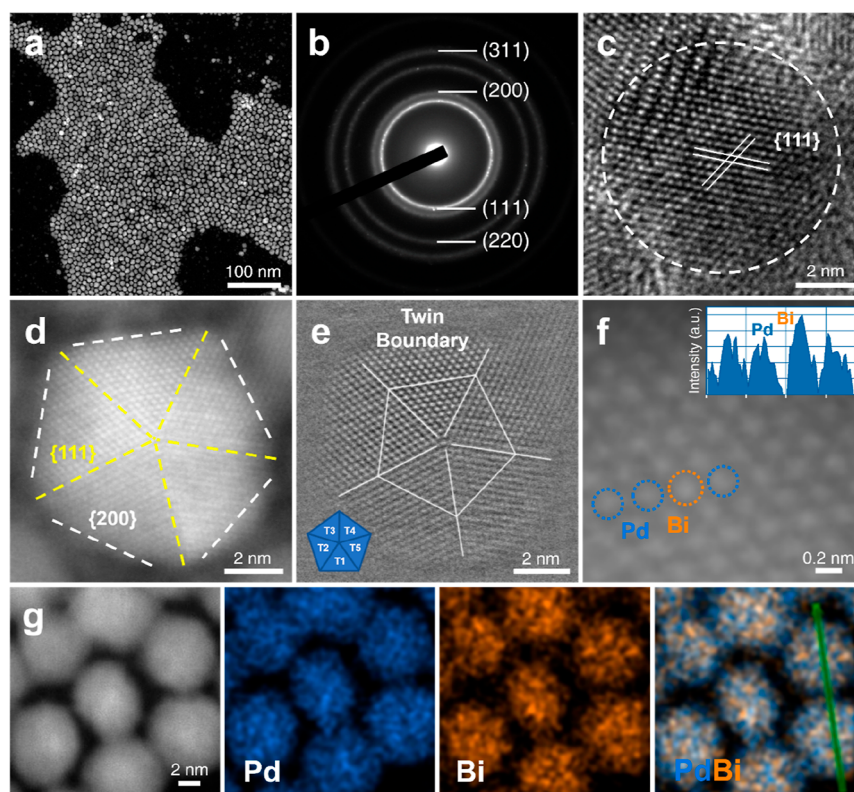

Figure 2. Aberration-corrected high-angle annular dark-field imaging (HAADF)-STEM images (a,d,f), SAED pattern (b), HRTEM images (c,e), and HAADF-STEM EDS (g) elemental mapping of Pd_8Bi NPs.

enhance the electrocatalytic mass activity, antitoxicity, and long-term stability, related to their inherent optimized electronic structure and morphological characteristics.[17,26−29]

Herein, we report an oil bath synthesis strategy to prepare monodisperse PdBi NPs with controllable sizes and compositions, including $Pd_{12}Bi$ NPs (7.0 nm), Pd_8Bi NPs (9.0 nm), and Pd_4Bi NPs (6.1 nm). The PdBi NPs were prepared in the presence of $Pd(acac)_2$ and $Bi(NO_3)_3·5H_2O$ as the precursors, hexadecyltrimethylammonium bromide (CTAB) as the structure-directing agent, L-ascorbic acid (AA) as the reducing agent, and N,N-dimethylformamide (DMF) as the solvent. Pd_8Bi NPs can reach the electrocatalytic mass activity of 2020 mA mg_{Pd}^{-1} toward EOR, approximately 4 times higher than the Pd/C (508 mA mg_{Pd}^{-1}) counterpart. Through precise control of the catalytic temperature, pH value, and C_2H_5OH concentration, the electrocatalytic mechanism of PdBi NPs for EOR was explored. DFT calculation shows that Pd_8Bi NPs present the lowest reaction barrier, leading to the higher mass activity of ethanol oxidation.

2. EXPERIMENTAL SECTION

2.1. Synthesis of PdBi NPs. In a typical synthesis of PdBi NPs, certain amounts of $Bi(NO_3)_3·5H_2O$ and CTAB (100 mg) were dissolved in 10 mL of DMF, kept stirring, and heated to 90 °C for 20 min. 30 mg of $Pd(acac)_2$ was dissolved in 5 mL of DMF, and 80 mg of AA was dissolved in another 5 mL of DMF under ultrasonic conditions. Then, 5 mL of $Pd(acac)_2$ was added in the above solution and kept stirring for 20 min. Afterward, 5 mL of AA was added in the above solution and kept stirring for 1 h. The black products were collected by centrifugation at 10 000 rpm for 8 min and washed with the mixed solution of ethanol and cyclohexane thoroughly, followed by the drying process in a vacuum oven at 60 °C for 6 h. The amounts of $Bi(NO_3)_3·5H_2O$ in the synthetic solutions were 3.98, 5.97, and 11.94 mg, respectively, and the corresponding PdBi products were marked as $Pd_{12}Bi$ NPs, Pd_8Bi NPs, and Pd_4Bi NPs, respectively.

2.2. Electrochemical Measurements. All electrochemical measurements were conducted in typical three-electrode cells at a controlled temperature, utilizing a CHI660 workstation. The detailed description was shown in our recent reports.[30]

2.3. First-Principles Calculations. The density functional theory (DFT) calculations in the framework were carried out based on the Dmol[3] code. The exchange−correlation functional under the generalized gradient approximation and Perdew−Burke−Ernzerhof

functional were adopted to describe the electron−electron interaction (see the Supporting Information online for more details).

3. RESULTS AND DISCUSSION

3.1. Crystal Structure Characterizations. The synthesis route of the PdBi NPs is shown in Figure S1. In the transmission electron microscopy (TEM) images (Figure 1 and Figures S2−S4), all the PdBi NPs are highly monodisperse. The average sizes of $Pd_{12}Bi$ NPs, Pd_8Bi NPs, and Pd_4Bi NPs are about 7.0, 9.0, and 6.1 nm (Figure S5), respectively, associated with the content of bismuth.

To further identify the intrinsic structure of bimetallic PdBi NP catalysts, a number of characterizations are utilized to analyze the physical structures of the NPs. Scanning transmission electron microscopy (STEM) images in Figures 2a and S6 show that the NPs are well dispersed and uniform in size. The selected-area electron diffraction (SAED) patterns in the insets of Figures 2b and S7 show the well-crystalline nature of the PdBi NPs, where the diffraction patterns were identified as Pd, including (111), (200), (220), and (311).[31] Most of PdBi NPs are single-crystalline, and an individual NP is displayed in the TEM image (Figure 2c), where the lattice spacing of the (111) plane is measured to be about 2.32 Å.

Some NPs show a twinning configuration, such as a symmetric fivefold twinned (SFT) NP, as shown in Figure 2d,e. The SFT-NP has a symmetric structure with five equal-length (111) twin interfaces and (200) edges, and the pole of SFT is located at the center of the SFT-NP.[32] The structural model of this SFT crystal is presented in the inset of Figure 2e, which consists of five identical subunits named T1−T5. In Figure 2f, some atoms (in orange circles) with relatively larger sizes have relatively higher intensity ratios and brightness than the other ones (in blue circles) with smaller sizes.[33] The twinning configuration should provide more active sites and boost the electrochemical performance of catalysts. Generally, due to the high sensitivity of HAADF to the changes in the atomic number of elements, brighter atoms have a larger average atomic number.[33,34] Further, there is a difference between the atomic number of Pd (atomic number 46) and Bi (atomic number 83). Therefore, the atoms in the blue and orange circles could be assigned to Bi and pure Pd, respectively. STEM energy-dispersive X-ray spectroscopy (STEM-EDS) elemental mapping (Figures 2g and S8 and S9), high-resolution line-scan EDS analysis (Figure S10), and scanning electron microscopy EDS (SEM−EDS, Figures S11−S13) data show that both Pd and Bi elements are uniformly distributed in the NPs, where palladium is the main element and relatively small amounts of bismuth can be clearly observed.

The powder X-ray diffraction (PXRD) patterns in Figure 3a,b reveal the characteristic diffraction peaks of PdBi NPs. The diffraction peaks of Pd_4Bi NF appear at 39.30, 49.14, 66.94, and 80.44°, corresponding to the (111), (200), (220), and (311) planes of Pd (JCPDS no. 46-1043) face-centered cubic (fcc) crystal phases ($Fm\overline{3}m$; a = 0.389 nm; ICDD 00-005-0681), respectively.[33,35] Meanwhile, no characteristic peak of Bi (JCPDS 26-2014) could be observed, implying that Bi atoms in the PdBi NPs were crystallized in an fcc phase.[24] Four typical direction peaks of PdBi NPs shifted to smaller angles with more Bi content, indicating the slight lattice expansion in the PdBi structure and the substitution of larger Bi atoms (atomic radius: 1.70 Å) for Pd atoms (atomic radius: 1.37 Å).[24] These indicate that the alloyed PdBi structure is formed.
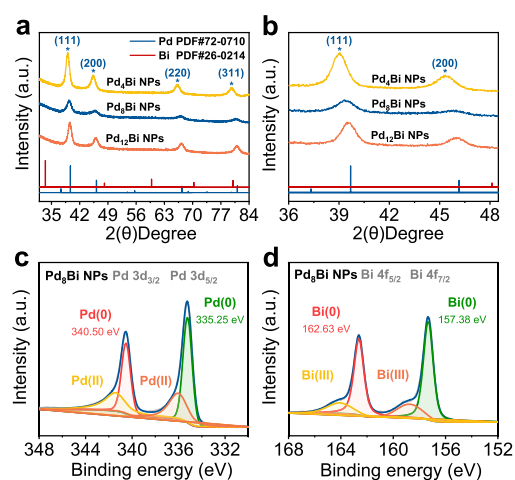

Figure 3. (a,b) PXRD patterns of $Pd_{12}Bi$ NPs, Pd_8Bi NPs, and Pd_4Bi NPs. (c,d) X-ray photoelectron spectroscopy (XPS) spectra of Pd_8Bi NPs.

XPS was carried out to investigate the binding states of PdBi NPs (Figures 3c,d, and S14). A pair of peaks at ∼335.25 and ∼340.50 eV is indexed to the Pd $3d_{5/2}$ and Pd $3d_{3/2}$ states, while another pair of peaks at ∼157.38 and ∼162.63 eV is indexed to Bi $4f_{7/2}$ and Bi $4f_{5/2}$ states. The spectra of Bi $4f_{7/2}$ are also split into two peaks, relating to Bi (0) (157.38 eV) and Bi (III) (158.75 eV).[17,25,36] It can be observed that both the Pd element and Bi element mainly exist in the form of zero valences. The as-prepared PdBi NPs may have a multicomponent structure, containing bimetallic PdBi as well as hydroxide $Bi(OH)_3$. A small amount of bismuth hydroxide is observed in ex situ XPS spectra as bismuth is hydrolyzed probably during chemical synthesis.[23]

3.2. Exploring the Synthesis Mechanism of Pd_8Bi NPs. To investigate the synthesis mechanism of Pd_8Bi NPs, the intermediates were collected at different times ranging from 15 min to 6 h, characterized by TEM, SEM-EDS, and PXRD. Clearly, the TEM images (Figures 4 and S17-S24) display that the sizes of PdBi NPs become larger as the experiment proceeds. The Pd_8Bi NPs are highly monodispersed initially, and the sizes range from 6.0 nm at 15 min to 9.1 nm at 1 h (ca. 1.0 nm per 15 min) and keep for the next few hours. The SEM-EDS (Figure S15) and PXRD (Figure S16) results demonstrate that Pd and Bi are formed simultaneously as the atomic percentage of the two elements remained unchanged, and the diffraction peaks have not shifted during the whole synthesis process. The reducing agent, that is, AA, plays a significant role in the co-reduction process due to the difference between the reduction potential of Pd and Bi. It can be summarized that the PdBi NPs containing Pd and Bi atoms are formed in the initial stage and gradually grow to a certain size as the reaction time increases.

3.3. Electrochemical Measurements and Analysis. Motivated by the monodisperse alloyed PdBi NP structure with high specific surface areas, we choose EOR as a model to evaluate their electrocatalytic performance. The possible mechanisms for EOR of the PdBi NP catalysts include the following elementary reactions based on a dual-pathway mechanism, as shown in Figure 5a.[37,38] The ideal complete oxidation of ethanol to carbon dioxide takes place through a 12 electron-transfer reaction, denoted as the C_1 pathway, requiring an extremely large energy (eq 1). In situ IR
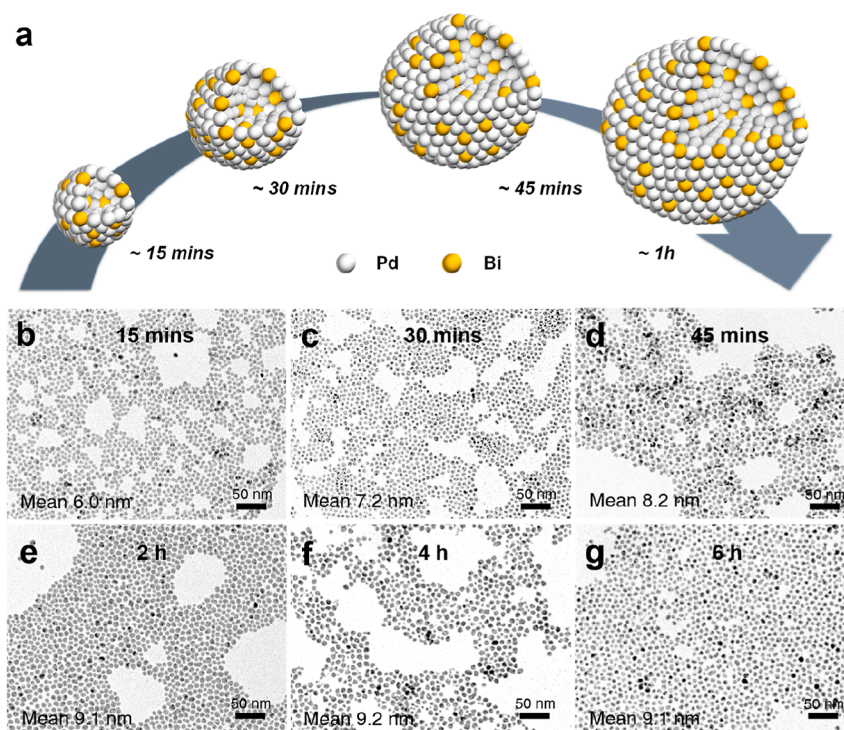
Figure 4. Schematic illustration of the possible structural evolution of Pd_8Bi NPs (a). TEM images of intermediates collected from the synthesis system for Pd_8Bi NPs at reaction times of 15 (b), 30 (c), 45 (d), 1 (e), 4 (f), and 6 h (g).
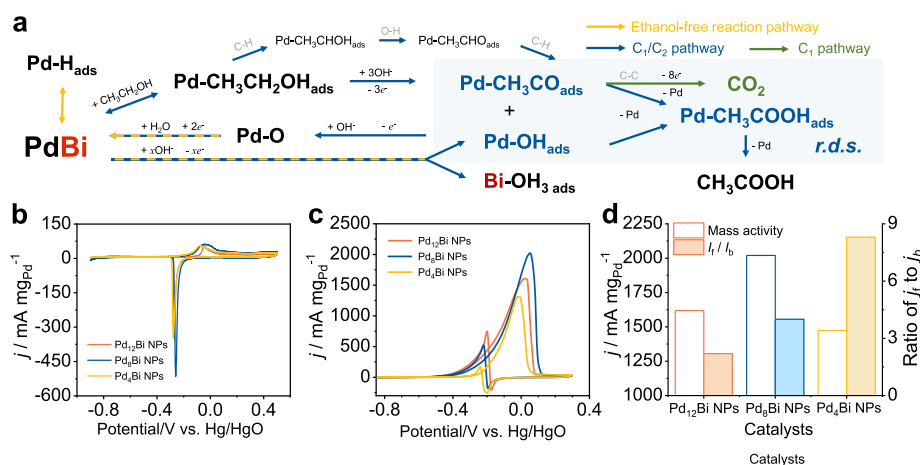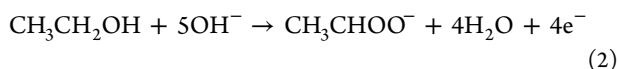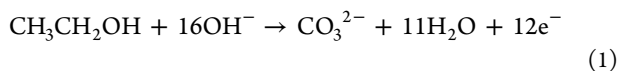

Figure 5. Possible mechanism for the EOR of PdBi NP catalysts in alkaline medium (a). Cyclic voltammetry (CV) curves (b,c), mass activities, and j_f/j_b ratios (d) of PdBi NPs in an aqueous 1 M KOH solution (b) or 1 M KOH/1 M C_2H_5OH solution (c).

characterization showed that the mechanism toward EOR is mainly a four-electron-transfer reaction denoted as the C_2 pathway (eq 2).[37,39]

$$CH_3CH_2OH + 16OH^- \rightarrow CO_3^{2-} + 11H_2O + 12e^- \tag{1}$$

$$CH_3CH_2OH + 5OH^- \rightarrow CH_3COO^- + 4H_2O + 4e^- \tag{2}$$

CV curves of PdBi NPs and Pd/C in 1 M KOH electrolyte are presented in Figures 5b and S25a. The typical adsorption/desorption region of hydrogen was limited by the presence of bismuth between −0.85 and −0.65 V.[37] The presence of bismuth clearly affects the shape of the CV to a certain extent by limiting the hydrogen adsorption/absorption processes on Pd at low potentials, followed by the change of the oxidation

processes at high potentials. During forward scanning, Pd would oxidize to Pd-O oxide film at a relatively higher potential. Afterward, the Pd-O oxide film was reduced back to Pd between −0.30 and −0.10 V in the reverse scan, where ECSA values can be calculated by the coulometric charge, as summarized in Table S1.[40,41] The ECSA values of $Pd_{12}Bi$ NPs, Pd_8Bi NPs, and Pd_4Bi NPs are about 36.4, 63.8, and 48.2 m^2 g_{Pd}^{-1}, respectively. Among them, Pd_8Bi NPs display the largest ECSA, approximately 4.8 times higher than the commercial Pd/C counterparts (13.4 m^2 g_{Pd}^{-1}).

The electrocatalytic activities of PdBi NPs and commercial Pd/C catalysts were compared in 1 M KOH + 1 M C_2H_5OH solution, as shown in Figures 5c and S25b. The ethanol molecules (C_2H_5OH) and OH^- would absorb on the PdBi NP catalysts quickly (eqs 3−5).
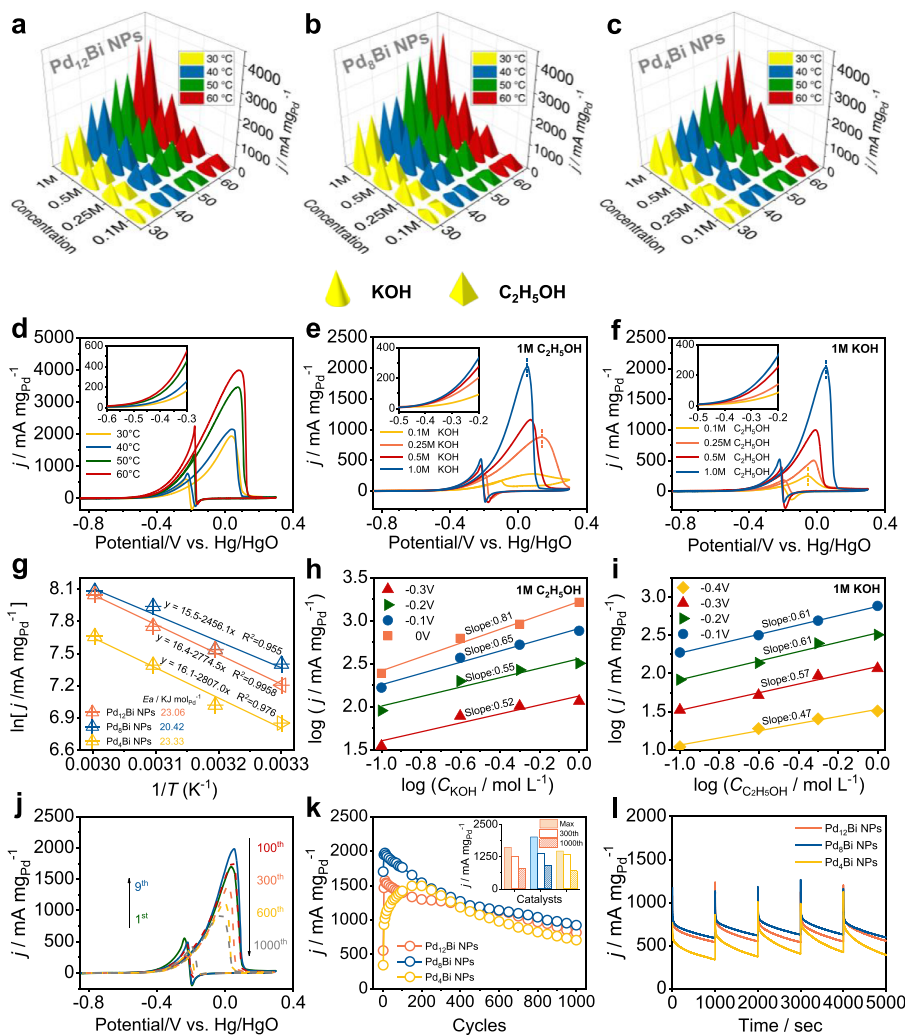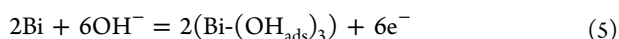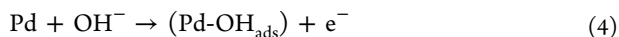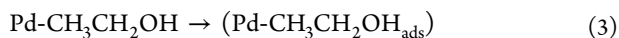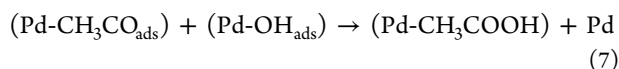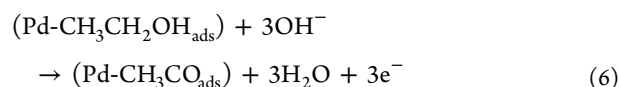
Figure 6. Current densities (a−c) and CV curves (d−f) of PdBi NPs in KOH/C$_2$H$_5$OH solutions with different electrocatalytic temperatures, KOH, and C$_2$H$_5$OH concentrations. Arrhenius plots (g) of Pd$_8$Bi NPs in 1 M KOH/C$_2$H$_5$OH solutions at different catalytic temperatures. CV curves of Pd$_8$Bi NPs in 1 M C$_2$H$_5$OH (e) or 1 M KOH (f) solutions with different KOH or C$_2$H$_5$OH concentrations at 30 °C, respectively. Plots of log j versus log C_{KOH} (h) and plots of log j versus log $C_{C_2H_5OH}$ (i) of PdBi NP-modified GCEs in 1 M ethanol/KOH (with different KOH/ethanol concentrations). The long-term CV curves (j), variation of current densities with cycles (k), and chronoamperometry (CA) curves (l) of Pd$_8$Bi NPs.

$$Pd\text{-}CH_3CH_2OH \rightarrow (Pd\text{-}CH_3CH_2OH_{ads}) \qquad (3)$$

$$Pd + OH^- \rightarrow (Pd\text{-}OH_{ads}) + e^- \qquad (4)$$

$$2Bi + 6OH^- = 2(Bi\text{-}(OH_{ads})_3) + 6e^- \qquad (5)$$

During anodic scanning, ethanol adsorbent (Pd-C$_2$H$_5$OH$_{ads}$) would oxidize to acetaldehyde adsorbent (Pd-CH$_3$CO$_{ads}$) with OH$^-$ step by step through three-electron transfer (possible mechanism: Pd-C$_2$H$_5$OH$_{ads}$ → Pd-CH$_3$CHOH$_{ads}$→Pd-CH$_3$CHO$_{ads}$→Pd-CH$_3$CO$_{ads}$), between −0.80 and −0.40 V (eq 6). The acetaldehyde adsorbent (Pd-CH$_3$CO$_{ads}$) and hydroxyl adsorbent (Pd-OH$_{ads}$) would react to form acetic acid adsorbent (Pd-CH$_3$COOH$_{ads}$) (eq 7), where lots of fresh Pd are exposed.[38,39,42] This is the rate-determining step of the EOR between −0.40 and 0.05 V. After this, a large number of acetic acid adsorbents form, and the current density increases as fresh Pd is exposed (eq 8).[40,42] Most of the fresh Pd are exposed at the potential of ca. 0.04 V, denoted as j_f. The mass activity (Figure 5d) of Pd$_{12}$Bi NPs, Pd$_8$Bi NPs, and Pd$_4$Bi NPs is 1619, 2020, and 1474 mA mg$_{Pd}^{-1}$, respectively, much higher

than that of Pd/C (508 mA mg$_{Pd}^{-1}$). The second metal element like Bi might play vital roles, including strain effect, ligand effect, geometric effect, and bifunctional effect. It is clear that the EOR activity is affected by the doping content of Bi.[6,42,43]

On further anodic scanning, the current density drops dramatically to zero between 0.04 and 0.3 V because the oxidation of Pd to the oxide film Pd-O would block the catalytic reaction. Meanwhile, the current density drops slowly as the doping content of Bi increases, and this is explained by the competition between the formation of (Pd-OH$_{ads}$) and (Bi-(OH$_{ads}$)$_3$).[22] When the content of Bi increases, the ratio of the concentration of (Pd-OH$_{ads}$) to (Bi-(OH$_{ads}$)$_3$), that is, c (Pd-OH$_{ads}$)/c (Bi-(OH$_{ads}$)$_3$) decreases, and fewer Pd-O is formed.

$$(Pd\text{-}CH_3CH_2OH_{ads}) + 3OH^-$$
$$\rightarrow (Pd\text{-}CH_3CO_{ads}) + 3H_2O + 3e^- \qquad (6)$$

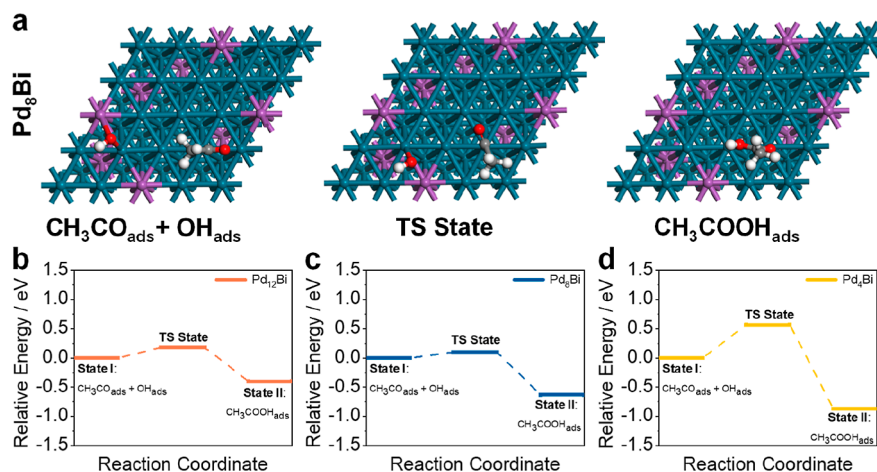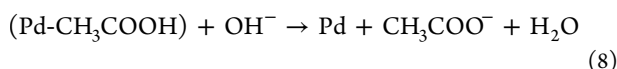$$(Pd\text{-}CH_3CO_{ads}) + (Pd\text{-}OH_{ads}) \rightarrow (Pd\text{-}CH_3COOH) + Pd \qquad (7)$$

Figure 7. Optimized intermediates and transition states in ethanol electro-oxidation of Pd_8Bi NPs (a). DFT-calculated TS energy profiles of $Pd_{12}Bi$ NPs (b), Pd_8Bi NPs (c), and Pd_4Bi NPs (d).

$$(\text{Pd-CH}_3\text{COOH}) + \text{OH}^- \rightarrow \text{Pd} + \text{CH}_3\text{COO}^- + \text{H}_2\text{O} \tag{8}$$

During the cathodic scanning, the current density increases rapidly at the potential of ca. −0.22 V, denoted as j_b, where much of carbon-containing (e.g., Pd-CH_3CHOH_{ads}, Pd-CH_3CO_{ads}, etc.) and oxygen-containing (e.g., Pd-O, etc.) toxic intermediates would be removed, and lots of fresh Pd would be exposed again. The higher values of the ratio of j_f to j_b, that is, j_f/j_b, denote the antitoxicity of the PdBi NP catalysts.[43] The j_f/j_b values of $Pd_{12}Bi$ NPs, Pd_8Bi NPs, and Pd_4Bi NPs are 2.2, 4.0, and 8.3, respectively. It is noted that the ratio of j_f/j_b increases with more doped Bi as less Pd-O is produced. The involved Bi atoms have higher affinity to adsorb OH^- from the electrolyte that is beneficial to the consecutive oxidation reaction of the C_2 intermediate ($C_2H_5OH \rightarrow CH_3CHOH \rightarrow CH_3CHO \rightarrow CH_3CO$) discussed above, that is, the bifunctional mechanism. The good antitoxic nature of PdBi NPs can be explained by the bifunctional mechanism.

Appropriate reaction temperature and medium conditions are favorable for the catalytic reaction.[8,44,45] In Figures 6a−c, S26, and Table S2, it is clear that higher electrocatalytic temperature and higher KOH (higher pH value) or ethanol concentration would favor the electrocatalysis of PdBi NPs on EOR. On the contrary, the electrocatalytic activity turns lower.

A higher catalytic temperature would activate Pd reaction sites, leading to better mass activity, as shown in Figure 6d. The activation energies (Ea) on EOR of $Pd_{12}Bi$ NPs, Pd_8Bi NPs, and Pd_4Bi NPs are calculated to be 23.06, 20.42, and 23.33 kJ mol_{Pd}^{-1}, respectively, with the Arrhenius plots (Figure 6g) according to the Arrhenius formula ($j = Ae^{-Ea/RT}$).[6] Among the PdBi NPs, the Pd_8Bi NPs exhibit the lowest activation energy.

Clearly, both the concentrations of KOH and ethanol have a dramatic effect on EOR, and the corresponding catalytic electrocatalytic mass activity at steady state is as follows (eq 9).[37]

$$j = nFKC_{C_2H_5OH}{}^M C_{KOH}{}^N \tag{9}$$

where j is the current at a specific potential, n is the electron-transfer number, F is faradic constant, and K is the reaction constant of EOR.

A higher concentration of KOH (Figure 6e) would lead to a higher oxidation current. As the concentration of KOH increases, the surface of PdBi NPs would be covered by more OH^-, followed by an acceleration of the formation of (Pd-OH_{ads}) and the oxidation of (Pd-$C_2H_5OH_{ads}$) to (Pd-CH_3CO_{ads}) step by step. Therefore, higher concentrations of (Pd-OH_{ads}) and (Pd-CH_3CO_{ads}) accelerate the rate-determining step on EOR. It can be observed that the corresponding potential of the forward peak (j_f) shifted negatively and dropped sharply as the concentration of OH^- increases due to the promotion of the formation of Pd-O.[38,41] Plots of the logarithm of mass activity versus log C_{KOH} of Pd_8Bi NPs in fixed 1 M ethanol are shown in Figure 6h. The values of currents increase as the values of C_{KOH} increase at varied potential ranges. Equation 9 can be rewritten as (eq 10)

$$\log(j) = \log(nFKC_{C_2H_5OH}{}^M) + N\log(C_{KOH}) \tag{10}$$

When the ethanol concentration (1 M) and electrode potential are held constant, we have (eqs 11 and 12)

$$\log(j) = A + N\log(C_{KOH}) \tag{11}$$

$$A = \log(nFKC_{C_2H_5OH}{}^M) \tag{12}$$

where A is a new constant.

A higher concentration of ethanol (Figure 6f) would lead to a higher electrocatalytic mass activity. The higher concentration of Pd-$C_2H_5OH_{ads}$ promotes the subsequent oxidation of Pd-$C_2H_5OH_{ads}$ to Pd-CH_3CO_{ads}, followed by the promotion of EOR. Clearly, the potential of the j_f shifts positively as the concentration of ethanol increases. This may be because a greater driving force is required to achieve a higher mass activity as the concentration of ethanol increases. Plots of the logarithm of mass activity versus log $C_{C_2H_5OH}$ of Pd_8Bi NPs in fixed 1 M KOH are shown in Figure 6i. The values of currents increase as the values of $C_{C_2H_5OH}$ increase at varied potentials (eq 13).

$$\log(j) = M\log(C_{C_2H_5OH}) + \log(nFKC_{KOH}{}^N) \tag{13}$$

When the KOH concentration (1 M) and the specific electrode potential are fixed, we have (eqs 14 and 15)

$$\log(j) = M\log(C_{C_2H_5OH}) + B \tag{14}$$

$$B = \log(nFKC_{KOH}{}^N) \tag{15}$$

where B is a new constant.

It is noticed that the ratio j_f/j_b increases with more Bi doping (Table S3), further indicating that the antitoxicity and durability of catalysis are deeply affected by the Bi element.

Figure 6j shows various CV curves of Pd$_8$Bi NPs with increasing cycle numbers. The electrocatalytic mass activity reaches the peak at the ninth cycle and then decreases gradually as the experiment proceeds. Clearly, the forward peak potential shifts positive first as higher energy is needed as more reactive sites are exposed and then shifts negative because these reactive sites are captured by the toxic intermediate and lower energy is required.[8,46] Also, the ratio of j_f/j_b turns to a lower value as the ability to clean toxic intermediates becomes weaker. PdBi NPs show a much better cycle stability than the commercial Pd/C counterpart, as shown in Figures 6k and S25c. Pd$_8$Bi NPs still possess 1151 mA mg$_{Pd}^{-1}$ after 1000 cycles. The size of Pd$_8$Bi NPs becomes irregular after 1000 cycles (Figure S27), which may be caused by the consumption of the catalyst surface. Figure 6l shows the long-term CA curves of the catalysts held at −0.1 V. It is clear that the Pd$_8$Bi NPs are always the highest and much higher than that of Pd$_{12}$Bi NPs, Pd$_4$Bi NPs, and commercial Pd/C (Figure S25d), further indicating that Pd$_8$Bi NPs possess a significantly enhanced electrocatalytic activity and stability.[47]

3.4. First-Principles Calculations. DFT calculation was carried out to further unveil the mechanism of alloyed PdBi NPs for EOR. The geometry optimization of the two constructed catalysts is shown in Figure S28. The hydroxyl adsorbent (Pd-OH$_{ads}$) and acetaldehyde adsorbent (Pd-CH$_3$CO$_{ads}$) are absorbed on the surface of the PdBi (111) lattice plane to form the acetic acid adsorbent (Pd-CH$_3$COOH$_{ads}$) (Figure 7a and S28−S30), where the rate-determining step of the EOR reacts.[40,48] We focused on this step of reaction calculation and discussed the effect of Bi doping on the electrocatalytic activity of the catalyst. The responding values of the reaction barrier are 0.18, 0.10, and 0.57 eV (Figure 7b−d), for Pd$_{12}$Bi NPs, Pd$_8$Bi NPs, and Pd$_4$Bi NPs, respectively. Pd$_8$Bi NPs possess the lowest values, which explain the highest electrocatalytic activity, consistent with the experimental results.[49]

4. CONCLUSIONS

Monodisperse alloyed PdBi NPs have been successfully synthesized, and the sizes are affected by the content of bismuth with the optimized electron structure. Among various PdBi NPs catalysts, the Pd$_8$Bi NPs exhibit a significantly enhanced mass activity (2020 mA mg$_{Pd}^{-1}$) and high stability for ethanol oxidation, much better than the commercial Pd/C counterpart. It is found that PdBi NP catalysts are more favorable for EOR under the conditions of higher catalytic temperature, higher pH values, as well as ethanol fuel concentrations. DFT calculation demonstrates the optimized electron structure, and the reaction barrier of the PdBi NPs boosts EOR. This study offers new insights into the design of noble-metal catalysts for enhanced catalytic activity and long-term durability.

ASSOCIATED CONTENT

ⓢ Supporting Information

The Supporting Information is available free of charge at https://pubs.acs.org/doi/10.1021/acsaem.1c03703.

Experimental section, TEM images, STEM images, SAED patterns, SEM−EDS patterns, XPS spectra, PXRD patterns, CV curves, and DFT calculations (PDF)

AUTHOR INFORMATION

Corresponding Authors

Yiqian Wang − *College of Physics, Qingdao University, Qingdao 266071, P. R. China;* ⓞ orcid.org/0000-0003-3341-7614; Email: yqwang@qdu.edu.cn

Aiping Fu − *College of Chemistry and Chemical Engineering, Qingdao University, Qingdao 266071, P. R. China;* Email: apfu@qdu.edu.cn

Peizhi Guo − *Institute of Materials for Energy and Environment, State Key Laboratory of Bio-Fibers and Eco-Textiles, College of Materials Science and Engineering, Qingdao University, Qingdao 266071, P. R. China;* ⓞ orcid.org/0000-0002-8773-2196; Email: pzguo@qdu.edu.cn, qduguo@163.com

Authors

Xianzhuo Lao − *Institute of Materials for Energy and Environment, State Key Laboratory of Bio-Fibers and Eco-Textiles, College of Materials Science and Engineering, Qingdao University, Qingdao 266071, P. R. China*

Min Yang − *Institute of Materials for Energy and Environment, State Key Laboratory of Bio-Fibers and Eco-Textiles, College of Materials Science and Engineering, Qingdao University, Qingdao 266071, P. R. China*

Xiaoli Sheng − *College of Physics, Qingdao University, Qingdao 266071, P. R. China*

Jing Sun − *Institute of Materials for Energy and Environment, State Key Laboratory of Bio-Fibers and Eco-Textiles, College of Materials Science and Engineering, Qingdao University, Qingdao 266071, P. R. China*

Derui Zheng − *Institute of Materials for Energy and Environment, State Key Laboratory of Bio-Fibers and Eco-Textiles, College of Materials Science and Engineering, Qingdao University, Qingdao 266071, P. R. China*

Mingyuan Pang − *Institute of Materials for Energy and Environment, State Key Laboratory of Bio-Fibers and Eco-Textiles, College of Materials Science and Engineering, Qingdao University, Qingdao 266071, P. R. China*

Hongliang Li − *Institute of Materials for Energy and Environment, State Key Laboratory of Bio-Fibers and Eco-Textiles, College of Materials Science and Engineering, Qingdao University, Qingdao 266071, P. R. China*

Complete contact information is available at:
https://pubs.acs.org/10.1021/acsaem.1c03703

Author Contributions

‖X.L. and M.Y. contributed equally to this work.

Notes

The authors declare no competing financial interest.

■ REFERENCES

(1) Zhang, J.; Ye, J.; Fan, Q.; Jiang, Y.; Zhu, Y.; Li, H.; Cao, Z.; Kuang, Q.; Cheng, J.; Zheng, J.; Xie, Z. Cyclic Penta-Twinned Rhodium Nanobranches as Superior Catalysts for Ethanol Electrooxidation. *J. Am. Chem. Soc.* **2018**, *140*, 11232−11240.

(2) Li, J.; Jilani, S. Z.; Lin, H.; Liu, X.; Wei, K.; Jia, Y.; Zhang, P.; Chi, M.; Tong, Y. J.; Xi, Z.; Sun, S. Ternary CoPtAu Nanoparticles as a General Catalyst for Highly Efficient Electro-oxidation of Liquid Fuels. *Angew. Chem., Int. Ed.* **2019**, *58*, 11527−11533.

(3) Yin, P. F.; Zhou, M.; Chen, J.; Tan, C.; Liu, G.; Ma, Q.; Yun, Q.; Zhang, X.; Cheng, H.; Lu, Q.; Chen, B.; Chen, Y.; Zhang, Z.; Huang, J.; Hu, D.; Wang, J.; Liu, Q.; Luo, Z.; Liu, Z.; Ge, Y.; Wu, X. J.; Du, X. W.; Zhang, H. Synthesis of Palladium-Based Crystalline@Amorphous Core-Shell Nanoplates for Highly Efficient Ethanol Oxidation. *Adv. Mater.* **2020**, *32*, 2000482.

(4) Du, R.; Wang, J.; Wang, Y.; Hübner, R.; Fan, X.; Senkovska, I.; Hu, Y.; Kaskel, S.; Eychmüller, A. Unveiling Reductant Chemistry in Fabricating Noble Metal Aerogels for Superior Oxygen Evolution and Ethanol Oxidation. *Nat. Commun.* **2020**, *11*, 1590.

(5) Li, C.; Yuan, Q.; Ni, B.; He, T.; Zhang, S.; Long, Y.; Gu, L.; Wang, X. Dendritic Defect-Rich Palladium-Copper-Cobalt Nanoalloys as Robust Multifunctional Non-Platinum Electrocatalysts for Fuel Cells. *Nat. Commun.* **2018**, *9*, 3702.

(6) Sun, L.; Lv, H.; Wang, Y.; Xu, D.; Liu, B. Unveiling Synergistic Effects of Interstitial Boron in Palladium-Based Nanocatalysts for Ethanol Oxidation Electrocatalysis. *J. Phys. Chem. Lett.* **2020**, *11*, 6632−6639.

(7) Zhang, Q.; Yin, Y. All-Inorganic Metal Halide Perovskite Nanocrystals: Opportunities and Challenges. *ACS Cent. Sci.* **2018**, *4*, 668−679.

(8) Sun, J.; Lao, X.; Yang, M.; Fu, A.; Chen, J.; Pang, M.; Gao, F.; Guo, P. Alloyed Palladium-Lead Nanosheet Assemblies for Electrocatalytic Ethanol Oxidation. *Langmuir* **2021**, *37*, 14930−14940.

(9) Luo, M.; Zhao, Z.; Zhang, Y.; Sun, Y.; Xing, Y.; Lv, F.; Yang, Y.; Zhang, X.; Hwang, S.; Qin, Y.; Ma, J.-Y.; Lin, F.; Su, D.; Lu, G.; Guo, S. PdMo Bimetallene for Oxygen Reduction Catalysis. *Nature* **2019**, *574*, 81−85.

(10) Li, J.; Yin, H.-M.; Li, X.-B.; Okunishi, E.; Shen, Y.-L.; He, J.; Tang, Z.-K.; Wang, W.-X.; Yücelen, E.; Li, C.; Gong, Y.; Gu, L.; Miao, S.; Liu, L.-M.; Luo, J.; Ding, Y. Surface evolution of a Pt-Pd-Au electrocatalyst for stable oxygen reduction. *Nat. Energy* **2017**, *2*, 17111.

(11) Bao, Y.; Liu, H.; Liu, Z.; Wang, F.; Feng, L. Pd/FeP Catalyst Engineering via Thermal Annealing for Improved Formic Acid Electrochemical Oxidation. *Appl. Catal., B* **2020**, *274*, 119106.

(12) Yang, M.; Lao, X.; Sun, J.; Ma, N.; Wang, S.; Ye, W.; Guo, P. Assembly of Bimetallic PdAg Nanosheets and Their Enhanced Electrocatalytic Activity toward Ethanol Oxidation. *Langmuir* **2020**, *36*, 11094−11101.

(13) Luo, L.; Fu, C.; Yan, X.; Shen, S.; Yang, F.; Guo, Y.; Zhu, F.; Yang, L.; Zhang, J. Promoting Effects of Au Submonolayer Shells on Structure-Designed Cu-Pd/Ir Nanospheres: Greatly Enhanced Activity and Durability for Alkaline Ethanol Electro-Oxidation. *ACS Appl. Mater. Interfaces* **2020**, *12*, 25961−25971.

(14) Gao, F.; Zhang, Y.; Ren, F.; Shiraishi, Y.; Du, Y. Universal Surfactant-Free Strategy for Self-Standing 3D Tremella-Like Pd-M (M = Ag, Pb, and Au) Nanosheets for Superior Alcohols Electrocatalysis. *Adv. Funct. Mater.* **2020**, *30*, 2000255.

(15) Zhao, F.; Li, C.; Yuan, Q.; Yang, F.; Luo, B.; Xie, Z.; Yang, X.; Zhou, Z.; Wang, X. Trimetallic Palladium-Copper-Cobalt Alloy Wavy Nanowires Improve Ethanol Electrooxidation in Alkaline Medium. *Nanoscale* **2019**, *11*, 19448−19454.

(16) Wang, L.; Wu, W.; Lei, Z.; Zeng, T.; Tan, Y.; Cheng, N.; Sun, X. High-performance alcohol electrooxidation on Pt3Sn-SnO2 nanocatalysts synthesized through the transformation of Pt-Sn nanoparticles. *J. Mater. Chem. A* **2020**, *8*, 592−598.

(17) Wang, Y.; Sun, D.; Chowdhury, T.; Wagner, J. S.; Kempa, T. J.; Hall, A. S. Rapid Room-Temperature Synthesis of a Metastable Ordered Intermetallic Electrocatalyst. *J. Am. Chem. Soc.* **2019**, *141*, 2342−2347.

(18) Luo, S.; Chen, W.; Cheng, Y.; Song, X.; Wu, Q.; Li, L.; Wu, X.; Wu, T.; Li, M.; Yang, Q.; Deng, K.; Quan, Z. Trimetallic Synergy in Intermetallic PtSnBi Nanoplates Boosts Formic Acid Oxidation. *Adv. Mater.* **2019**, *31*, 1903683.

(19) Seh, Z. W.; Kibsgaard, J.; Dickens, C. F.; Chorkendorff, I.; Norskov, J. K.; Jaramillo, T. F. Combining Theory and Experiment in Electrocatalysis: Insights into Materials Design. *Science* **2017**, *355*, No. eaad4998.

(20) Wang, C.; Shang, H.; Wang, Y.; Xu, H.; Li, J.; Du, Y. Interfacial Electronic Structure Modulation Enables CoMoOx/CoOx/RuOx to Boost Advanced Oxygen Evolution Electrocatalysis. *J. Mater. Chem. A* **2021**, *9*, 14601−14606.

(21) Wang, C.; Shang, H.; Li, J.; Wang, Y.; Xu, H.; Wang, C.; Guo, J.; Du, Y. Ultralow Ru Doping Induced Interface Engineering in MOF Derived Ruthenium-Cobalt Oxide Hollow Nanobox for Efficient Water Oxidation Electrocatalysis. *Chem. Eng. J.* **2021**, *420*, 129805.

(22) Zalineeva, A.; Serov, A.; Padilla, M.; Martinez, U.; Artyushkova, K.; Baranton, S.; Coutanceau, C.; Atanassov, P. B. Self-Supported PdxBi Catalysts for the Electrooxidation of Glycerol in Alkaline Media. *J. Am. Chem. Soc.* **2014**, *136*, 3937−3945.

(23) Yuan, X.; Zhang, Y.; Cao, M.; Zhou, T.; Jiang, X.; Chen, J.; Lyu, F.; Xu, Y.; Luo, J.; Zhang, Q.; Yin, Y. Bi(OH)3/PdBi Composite Nanochains as Highly Active and Durable Electrocatalysts for Ethanol Oxidation. *Nano Lett.* **2019**, *19*, 4752−4759.

(24) Hu, C.; Chen, Z.; Han, F.; Lin, Z.; Yang, X. Surface engineering of ultrasmall supported PdxBi nanoalloys with enhanced electrocatalytic activity for selective alcohol oxidation. *Chem. Commun.* **2019**, *55*, 13566−13569.

(25) Shen, T.; Chen, S.; Zeng, R.; Gong, M.; Zhao, T.; Lu, Y.; Liu, X.; Xiao, D.; Yang, Y.; Hu, J.; Wang, D.; Xin, H. L.; Abruña, H. D. Tailoring the Antipoisoning Performance of Pd for Formic Acid Electrooxidation via an Ordered PdBi Intermetallic. *ACS Catal.* **2020**, *10*, 9977−9985.

(26) Luo, M.; Guo, S. Strain-Controlled Electrocatalysis on Multimetallic Nanomaterials. *Nat. Rev. Mater.* **2017**, *2*, 17059.

(27) Yao, Y.; Gu, X.-K.; He, D.; Li, Z.; Liu, W.; Xu, Q.; Yao, T.; Lin, Y.; Wang, H.-J.; Zhao, C.; Wang, X.; Yin, P.; Li, H.; Hong, X.; Wei, S.; Li, W.-X.; Li, Y.; Wu, Y. Engineering the Electronic Structure of Submonolayer Pt on Intermetallic Pd3Pb via Charge Transfer Boosts the Hydrogen Evolution Reaction. *J. Am. Chem. Soc.* **2019**, *141*, 19964−19968.

(28) Yin, J.; Zhan, F.; Jiao, T.; Wang, W.; Zhang, G.; Jiao, J.; Jiang, G.; Zhang, Q.; Gu, J.; Peng, Q. Facile Preparation of Self-Assembled MXene@Au@CdS Nanocomposite with Enhanced Photocatalytic Hydrogen Production Activity. *Sci. China Mater.* **2020**, *63*, 2228−2238.

(29) Li, K.; Jiao, T.; Xing, R.; Zou, G.; Zhou, J.; Zhang, L.; Peng, Q. Fabrication of Tunable Hierarchical MXene@AuNPs Nanocomposites Constructed by Self-Reduction Reactions with Enhanced Catalytic Performances. *Sci. China Mater.* **2018**, *61*, 728−736.

(30) Yang, M.; Pang, M.; Chen, J.; Gao, F.; Li, H.; Guo, P. Surfactant-Assisted Synthesis of Palladium Nanosheets and Nanochains for the Electrooxidation of Ethanol. *ACS Appl. Mater. Interfaces* **2021**, *13*, 9830−9837.

(31) Wang, H.; Jiao, L.; Zheng, L.; Fang, Q.; Qin, Y.; Luo, X.; Wei, X.; Hu, L.; Gu, W.; Wen, J.; Zhu, C. PdBi Single-Atom Alloy Aerogels for Efficient Ethanol Oxidation. *Adv. Funct. Mater.* **2021**, *31*, 2103465.

(32) Song, M.; Wu, Z.; Lu, N.; Li, D. Strain Relaxation-Induced Twin Interface Migration and Morphology Evolution of Silver Nanoparticles. *Chem. Mater.* **2019**, *31*, 842−850.

(33) Gunji, T.; Noh, S. H.; Tanabe, T.; Han, B.; Nien, C. Y.; Ohsaka, T.; Matsumoto, F. Enhanced Electrocatalytic Activity of Carbon-Supported Ordered Intermetallic Palladium-Lead (Pd3Pb) Nanoparticles toward Electrooxidation of Formic Acid. *Chem. Mater.* **2017**, *29*, 2906−2913.

(34) Bu, L.; Tang, C.; Shao, Q.; Zhu, X.; Huang, X. Three-Dimensional Pd3Pb Nanosheet Assemblies: High-Performance Non-

Pt Electrocatalysts for Bifunctional Fuel Cell Reactions. *ACS Catal.* **2018**, *8*, 4569−4575.

(35) Tang, C.; Zhang, N.; Ji, Y.; Shao, Q.; Li, Y.; Xiao, X.; Huang, X. Fully Tensile Strained Pd3Pb/Pd Tetragonal Nanosheets Enhance Oxygen Reduction Catalysis. *Nano Lett.* **2019**, *19*, 1336−1342.

(36) Wang, Y.; Hall, A. S. Pulsed Electrodeposition of Metastable Pd31Bi12 Nanoparticles for Oxygen Reduction Electrocatalysis. *ACS Energy Lett.* **2019**, *5*, 17−22.

(37) Jiang, R.; Tran, D. T.; McClure, J. P.; Chu, D. A Class of (Pd-Ni-P) Electrocatalysts for the Ethanol Oxidation Reaction in Alkaline Media. *ACS Catal.* **2014**, *4*, 2577−2586.

(38) Liang, Z. X.; Zhao, T. S.; Xu, J. B.; Zhu, L. D. Mechanism Study of the Ethanol Oxidation Reaction on Palladium in Alkaline Media. *Electrochim. Acta* **2009**, *54*, 2203−2208.

(39) Kim, I.; Han, O. H.; Chae, S. A.; Paik, Y.; Kwon, S.-H.; Lee, K.-S.; Sung, Y.-E.; Kim, H. Catalytic Reactions in Direct Ethanol Fuel Cells. *Angew. Chem., Int. Ed.* **2011**, *50*, 2270−2274.

(40) Luo, L.; Fu, C.; Yang, F.; Li, X.; Jiang, F.; Guo, Y.; Zhu, F.; Yang, L.; Shen, S.; Zhang, J. Composition-Graded Cu-Pd Nanospheres with Ir-Doped Surfaces on N-Doped Porous Graphene for Highly Efficient Ethanol Electro-Oxidation in Alkaline Media. *ACS Catal.* **2019**, *10*, 1171−1184.

(41) Lao, X.; Yang, M.; Chen, J.; Zhang, L. Y.; Guo, P. The ethanol oxidation reaction on bimetallic PdxAg1-x nanosheets in alkaline media and their mechanism study. *Electrochim. Acta* **2021**, *374*, 137912.

(42) Du, W.; Mackenzie, K. E.; Milano, D. F.; Deskins, N. A.; Su, D.; Teng, X. Palladium-Tin Alloyed Catalysts for the Ethanol Oxidation Reaction in an Alkaline Medium. *ACS Catal.* **2012**, *2*, 287−297.

(43) Zhang, W.; Yang, Y.; Huang, B.; Lv, F.; Wang, K.; Li, N.; Luo, M.; Chao, Y.; Li, Y.; Sun, Y.; Xu, Z.; Qin, Y.; Yang, W.; Zhou, J.; Du, Y.; Su, D.; Guo, S. Ultrathin PtNiM (M = Rh, Os, and Ir) Nanowires as Efficient Fuel Oxidation Electrocatalytic Materials. *Adv. Mater.* **2019**, *31*, 1805833.

(44) Cohen, J. L.; Volpe, D. J.; Abruña, H. D. Electrochemical Determination of Activation Energies for Methanol Oxidation on Polycrystalline Platinum in Acidic and Alkaline Electrolytes. *Phys. Chem. Chem. Phys.* **2007**, *9*, 49−77.

(45) Wang, L.; Meng, H.; Shen, P. K.; Bianchini, C.; Vizza, F.; Wei, Z. In situFTIR spectroelectrochemical study on the mechanism of ethylene glycol electrocatalytic oxidation at a Pd electrode. *Phys. Chem. Chem. Phys.* **2011**, *13*, 2667−2673.

(46) Li, J.; Wang, C.; Shang, H.; Wang, Y.; You, H.; Xu, H.; Du, Y. Metal-modified PtTe2 nanorods: Surface reconstruction for efficient methanol oxidation electrocatalysis. *Chem. Eng. J.* **2021**, *424*, 130319.

(47) Wu, T.; Wang, X.; Emrehan Emre, A.; Fan, J.; Min, Y.; Xu, Q.; Sun, S. Graphene-Nickel Nitride Hybrids Supporting Palladium Nanoparticles for Enhanced Ethanol Electrooxidation. *J. Energy Chem.* **2021**, *55*, 48−54.

(48) Guo, Y.; Li, B.; Shen, S.; Luo, L.; Wang, G.; Zhang, J. Potential-Dependent Mechanistic Study of Ethanol Electro-oxidation on Palladium. *ACS Appl. Mater. Interfaces* **2021**, *13*, 16602−16610.

(49) Evans, E. J.; Li, H.; Han, S.; Henkelman, G.; Mullins, C. B. Oxidative Cross-Esterification and Related Pathways of Co-Adsorbed Oxygen and Ethanol on Pd-Au. *ACS Catal.* **2019**, *9*, 4516−4525.